Atomic-scale characterization of the $SrTiO_3$ $\Sigma3$ (112) $[\bar{1}10]$ grain boundary

K. J. Dudeck,[1] N. A. Benedek,[2,*] M. W. Finnis,[2] and D. J. H. Cockayne[1,†]
[1]*Department of Materials, University of Oxford, Parks Road, Oxford OX1 3JA, United Kingdom*
[2]*Department of Materials and Department of Physics, Imperial College London, Exhibition Road, London SW7 2AZ, United Kingdom*
(Received 3 March 2010; published 23 April 2010)

The strontium titanate $\Sigma3$ (112) $[\bar{1}10]$ grain boundary has been investigated using aberration-corrected high-resolution transmission electron microscopy and exit wave-function reconstruction. By quantitatively comparing the experimental exit wave phase with that expected from relaxed model structures obtained by density-functional theory, it has been possible to differentiate between two proposed structures not significantly different in their calculated energies, and to deduce information about three-dimensional atomic arrangements near the boundary using the reconstructed exit wave-function phase.

DOI: 10.1103/PhysRevB.81.134109 PACS number(s): 61.72.Mm, 42.30.Rx, 68.35.Ct, 68.37.Og

I. INTRODUCTION

Grain boundaries (GBs) play a critical role in determining the electronic and structural properties of polycrystalline $SrTiO_3$. In order to develop a robust understanding of these properties, a knowledge of the GB atomic structure is essential. Reliable first-principles modeling of high-symmetry GBs is possible and in conjunction with experimental characterization, can be used to verify the atomic-scale structure of the boundary. Of the several possible experimental techniques for determining GB structure, high-resolution transmission electron microscopy (HRTEM) is the most direct.[1]

There have been a small number of theoretical studies of grain boundaries in $SrTiO_3$. Kienzle *et al.*[2] studied the $SrTiO_3$ $\Sigma3(111)$ $[\bar{1}10]$ grain boundary by quantitatively comparing HRTEM images simulated from a number of model structures (generated using a technique similar to a genetic algorithm) with experimental images. The model structure was refined based on the results of the image comparison and converged toward a structure which yielded the best match with the experimental image. The authors also performed classical simulations (using an interatomic potential) of the boundary; however there were significant differences between the structure predicted by classical simulations and that generated by the image-matching algorithm. Hutt *et al.*[3] and Astala *et al.*[4] performed density-functional theory (DFT) calculations on the $\Sigma3$ (111) $[\bar{1}10]$ and $\Sigma5$ (001) $SrTiO_3$ boundaries. Although these authors noted generally good qualitative agreement between the structures predicted by DFT and those observed experimentally, no quantitative structural comparisons were made.

In this work the atomic structure of the $SrTiO_3$ $\Sigma3$ (112) $[\bar{1}10]$ GB has been studied using aberration-corrected HRTEM and exit plane-wave reconstruction. Through comparison of exit wave-function phase data simulated from model structures with the experimentally observed structure, a DFT refined model structure has been obtained.

Crystalline $SrTiO_3$ has a cubic, perovskite structure with lattice parameter $a_0=3.905$ Å at room temperature. The $\Sigma3$ (112) GB is a symmetric tilt boundary with a theoretical misorientation angle of 70.5° about $[\bar{1}10]$. In the bulk crystal the atomic planes parallel to the GB are spaced 0.8 Å apart and alternate in composition between Sr-Ti-O and O_2. First-principles DFT calculations modeling the stoichiometric $\Sigma3$ (112) grain boundary have been reported by Benedek *et al.*,[5] where full details concerning the calculations can be found. They also calculated the γ surface for the $\Sigma3$ (112) GB using a classical interatomic potential. The γ surface is a map of the constrained grain-boundary energy as a function of a vector, **t**, which defines the parallel translation of the adjacent grains. They found the same two distinct low-energy minima both with empirical and DFT methods, each minimum having a unique GB configuration (see Fig. 1). In one configuration the GB was mirror symmetric with no translation {which is defined as $\mathbf{t}=(0,0)$ $[11\bar{1}]$ $[\bar{1}10]$} while the other had mirror-glide symmetry [$\mathbf{t}=(2a_0/3,0)$ $[11\bar{1}]$ $[\bar{1}10]$]. With DFT, both configurations were calculated to have a GB energy of 1.06 J m^{-2} and the two states were the only minima on the γ surface.

II. EXPERIMENTAL METHOD

A $10\times10\times1$ mm^3 piece of bulk $SrTiO_3$ $\Sigma3$ (112) bicrystal material, prepared by diffusion bonding, was purchased from a commercial retailer (MaTecK GmbH). The bulk material was heat treated according to the following sequence: 1000 °C for 2 h in air; 1300 °C for 2 h in vacuum; 1300 °C for 2 h in argon; 1000 °C for 40 h in air. Following heat treatment, HRTEM specimens were prepared using the methods described by Strecker *et al.*[6] Experimental

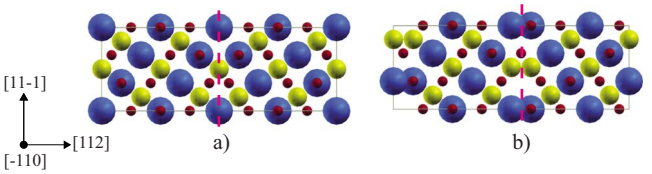

FIG. 1. (Color online) (a) Mirror symmetric configuration and (b) mirror-glide symmetric configuration. Blue spheres (dark gray) represent Sr, yellow spheres (light gray) represent Ti, red spheres (black) represent O, and the dashed line is the position of the GB. See Ref. 5 for further details.

HRTEM images were obtained using a JEOL 2200 MCO microscope operating at 200 kV and fitted with CEOS aberration correctors[7] on both the image and probe forming optics. Third-order spherical aberration (C_3) was set to balance fifth-order spherical aberration, $C_3=-6$ μm;[8] previous studies have used negative C_3 values to improve contrast of light elements such as oxygen.[9] Aberration coefficient values were measured using tilt-tableau series taken with tilt angles of up to 18 mrad. Diffraction patterns and goniometer tilt angles corresponding to two zone axis orientations for each grain were recorded and the quaternion representation of rotations, as implemented in the GROT code,[10] was used to find the best fit of the misorientation axis and angle to the experimental data, which was found to be $(71.9\pm0.5)°$ about $\langle 0.71\pm0.01 \;\; 0.70\pm0.01 \;\; 0\pm0.01\rangle$. Uncertainty values shown are considered to be upper limits, estimated from the accuracy of the goniometer tilt angles. This orientation is slightly off the ideal $\Sigma3$ (112) misorientation, and consequently the GB comprised coherent and incoherent segments. This study concentrated upon the coherent areas.

All experimental images were collected at a magnification of 1.5M with a pixel size of 0.008 nm/pixel. 20-member focal series data sets were collected using a focal step of 7 nm with defocus range straddling Gaussian defocus. Quantitative HRTEM image matching following the approach of Hÿtch and Stobbs[11] was employed in order to determine the specimen thickness and microscope defocus. Regions of the images containing only bulk crystal were quantitatively compared with simulated images using the cross-mean angle metric; complete details of the defocus-thickness matching process can be found in Ref. 12. Using the thickness values fitted from the bulk crystal (25 Å), images were simulated from both the proposed model structures shown in Fig. 1 and then quantitatively compared to the experimental images using the same metric. This analysis showed clearly that the mirror symmetric model provided the best match to the experimentally observed GB structure for all data sets.[12]

For data sets corresponding to sufficiently thin regions of the specimen, the focal series data sets were used to obtain the exit wave function, using the linear Wiener filter approach[13] implemented in the SEMPER image processing package;[14,15] the reconstruction algorithm also includes a procedure that compensates for the charge-coupled-device modulation transfer function (see Ref. 15 for complete details). Following reconstruction, the resultant exit wave functions were then digitally corrected for residual higher-order aberrations, using an approach similar to that presented in Ref. 16. For the areas analyzed in this work, there was very little amorphous material to use for quantitative aberration assessment, and therefore higher-order aberration values were determined manually by adjusting the aberrations in order to achieve the best possible agreement between the bulk crystal in the reconstructed wave-function phase and the simulated phase; twofold and threefold astigmatism and coma were adjusted. Further simulations were carried out to ensure that the specimen was sufficiently thin for the peaks in the reconstructed exit wave phase to correspond to atomic columns.

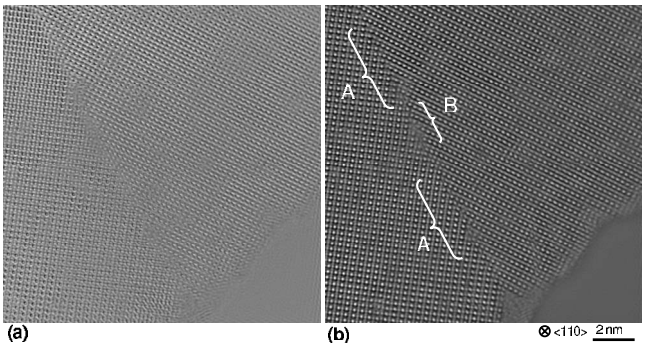

FIG. 2. Reconstructed exit wave function (a) modulus and (b) phase data obtained from one of the five thin areas analyzed. The coherent regions used for analysis are indicated by the brackets labeled "A" on the phase (these represent two of the five coherent segments used for analysis). The incoherent region, labeled "B," contains a secondary grain-boundary dislocation.

III. EXPERIMENTAL ANALYSIS

Figure 2 presents a typical exit wave-function modulus and phase corresponding to one of the data sets analyzed for this work. Four additional reconstructions were analyzed (from different thin regions of the specimen). In Fig. 2, the coherent and incoherent segments of the grain boundary are visible. The coherent segments used for analysis are indicated by brackets labeled "A" on the phase.

Figures 3(a) and 3(b) show two typical images from one of the focal series data sets while Fig. 3(c) shows the corresponding reconstructed exit wave phase with the positions of the Sr-O-Ti {112} planes indicated by arrows. The agreement with the simulated phase is not perfect, most likely due to the slight sample mistilt or surface roughness, but is sufficiently good for the purposes of this study. Due to the misorientation of the experimental specimen, both grains could not be aligned exactly onto a zone axis. However, analysis of simulated exit wave-function phase data from models tilted to angles consistent with those expected experimentally ($\leq0.5°$) indicate that, while tilting effects the qualitative agreement between the experimental and simulated data, it does not have a significant impact on the quantitative conclusions drawn in subsequent sections. Furthermore, analysis of the experimental phase data before and after correction of higher-order aberrations indicates that this correction does not have a significant impact on the quantitative conclusions.

Qualitative assessment of Fig. 3(c) indicates that there is a Sr-O-Ti {112} plane, rather than an O_2 plane, on the GB mirror plane, which is consistent with the mirror symmetric model structure. This is verified by comparing to the exit wave phase simulated from the mirror symmetric model structure, shown as an inset to Fig. 3(c). It is in agreement with the quantitative comparisons carried out using individual images from the focal series.[12]

In order to assess the agreement between the DFT relaxed structure and the experimentally observed structure, quantitative analysis was carried out on both the reconstructed exit wave phase and the exit wave phase simulated from the mirror symmetric model structure. As both the quantitative HRTEM image analysis and qualitative exit wave-function

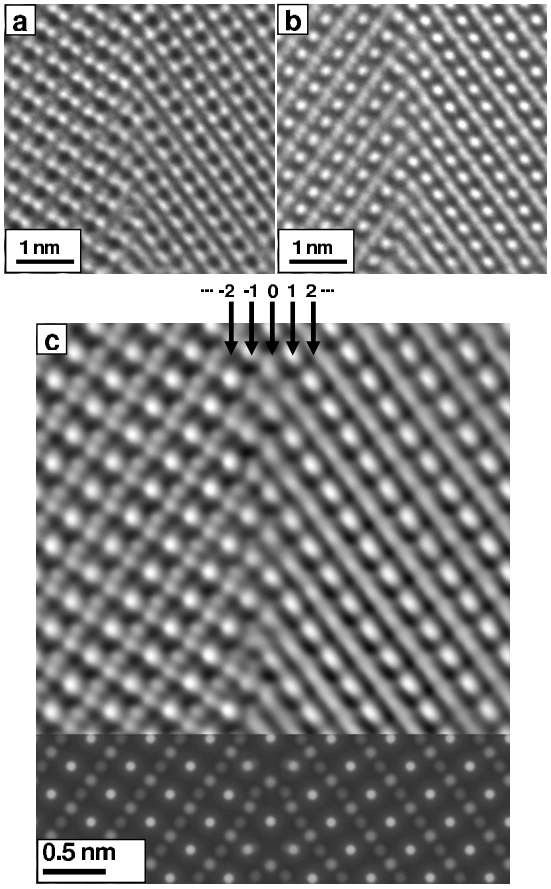

FIG. 3. Experimental images from a focal series of images having defocus values of (a) (-70 ± 10) Å and (b) $(+120 \pm 10)$ Å. (c) The reconstructed exit wave-function phase corresponding to data set of which images (a) and (b) are part. The lower portion of (c) shows a simulated exit wave phase for a thickness of 25 Å. The Sr-O-Ti {112} planes are indicated by arrows.

phase analysis indicate that the experimental GB structure is consistent with the mirror symmetric model, only this structure was analyzed quantitatively. The exit wave phase data was analyzed using a three step approach. First, positions of the Sr-O columns were determined with subpixel accuracy using a center-of-mass approach using the exit wave phase. Second, the mean value of pixels on Sr-O columns were calculated within a square subregion centered on the column position. The subregion used for the phase analysis had side lengths equal to the average full width at half maximum of the peaks corresponding to the Sr-O columns. Finally, pixel values measured on five or more Sr-O columns on a given Sr-O-Ti {112} plane were averaged to give the mean pixel values of Sr-O columns on each of the planes, indicated by arrows in Fig. 3(c). Uncertainty of the mean values was calculated as the standard deviation of the pixel values measured on the columns. Steps one and two were repeated for Sr-O columns in the bulk (considered as at least 3.5 nm away from the boundary plane) and the mean pixel value on all bulk Sr-O columns was calculated. This process was repeated for five coherent segments of the GB. Henceforth, the pixel values measured on the Sr-O columns from the exit wave phase will be referred to as phase measurements for simplicity.

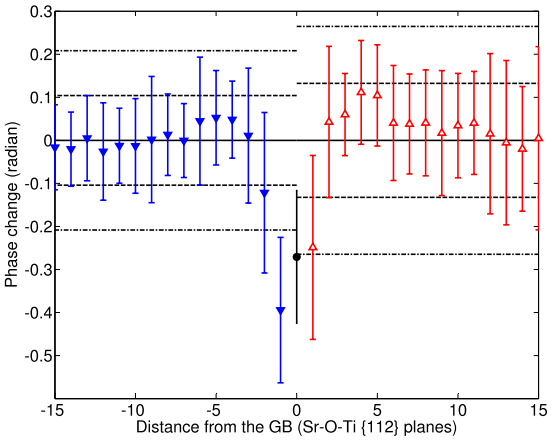

FIG. 4. (Color online) Experimentally measured average phase change with respect to mean bulk Sr-O column phase plotted as a function of distance from the GB. Filled triangles indicate Sr-O columns on planes to the left of the boundary mirror plane, open triangles indicate Sr-O columns to the right of the boundary mirror plane, and the filled circle indicates the Sr-O columns on the mirror plane. The dashed and dot-dashed lines are the $\pm 1\sigma$ and $\pm 2\sigma$ confidence intervals of the mean bulk Sr-O column phase. Distance from the GB is indexed as shown in Fig. 3(c).

Figure 4 presents the phase change measured on the Sr-O columns with respect to bulk Sr-O column phase, averaged from all five coherent regions. Data in Fig. 4 is plotted as a function of position with respect to the GB mirror plane using the plane indices indicated by the arrows in Fig. 3(c). From Fig. 4, it is observed that the phase measured on the Sr-O columns on the {112} planes *on and adjacent to* the boundary mirror plane show a statistically significant decrease with respect to the bulk Sr-O column phase. From Table I, the average phase change measured for the Sr-O columns on Sr-O-Ti {112} on and adjacent to the boundary mirror plane is (-0.29 ± 0.09) rad. All five thin areas analyzed showed consistent results; however, not all five areas included a decrease on both the mirror plane and adjacent planes.

IV. COMPARISON WITH DENSITY-FUNCTIONAL THEORY

Quantitative phase analysis was repeated on phases simulated from both the unrelaxed mirror symmetric model structure [i.e., the ideal $\Sigma 3$ (112) GB] and DFT relaxed mirror symmetric model structure for a model thickness of 25 Å. As can be seen from Fig. 5(a), the unrelaxed boundary shows no phase decrease on Sr-O columns across the boundary. However, a significant decrease is observed for the Sr-O columns on the Sr-O-Ti {112} planes adjacent to the boundary mirror plane for the stoichiometric DFT relaxed mirror symmetric model, as shown in Fig. 5(b). In the DFT model, the Sr-O atoms on the Sr-O-Ti {112} planes adjacent to the GB experience a significant rumpling. Rumpling is defined by Benedek *et al.*[5] as $r = Sr^{[112]} - O^{[112]}$, i.e., the difference in the position of the Sr and O atoms along [112]. For the Sr-O columns on the planes adjacent to the boundary they calcu-

TABLE I. Average phase change measured on Sr-O columns from the reconstructed exit wave phase (averaged over all five coherent segments) as well as the refined mirror symmetric DFT relaxed structure.

Column position	Experiment (rad)	Original DFT model[a] (rad)	Refined DFT model (rad)
Adjacent (left)	-0.39 ± 0.17	-0.30 ± 0.003	-0.30 ± 0.003
Mirror plane	-0.23 ± 0.12	-0.004 ± 0.003	-0.40 ± 0.003
Adjacent (right)	-0.25 ± 0.21	-0.30 ± 0.003	-0.30 ± 0.003

[a]Model originally published in Ref. 5.

late a rumpling of $r=0.5$ Å. The Sr-O rumpling decreases significantly ($r \leq 0.1$ Å) for planes further from the boundary (see Fig. 6 in Ref. 5).

In order to determine whether the Sr-O rumpling could be the cause of the experimentally observed phase change, exit wave functions were simulated from an unrelaxed GB model with rumpling added manually with several different values of r (using model thickness of 25 Å and rumpling all Sr and O atoms). It was assumed that the rumpling was symmetric about the unrelaxed column position, i.e., the Sr atoms were shifted by $+r/2$ and O atoms by $-r/2$, so that the total rumpling has magnitude r. (It should be noted that, in the case of the DFT relaxed model, the rumpling is not necessarily symmetric about the unrelaxed column position.) The phase change calculated as a function of rumpling is reported in Table II. While these results are for symmetric rumpling, we found that making the rumpling asymmetric did not change the results significantly. It is observed that rumpling can cause significant phase change, consistent with the values measured on the Sr-O columns on Sr-O-Ti {112} planes adjacent to the boundary mirror plane of the DFT model.

From the rumpling analysis presented in Table II, it is suggested that this phase change is due to the rumpling of the Sr and O atoms. While the experimentally observed phase decrease on the {112} planes adjacent to the GB can be explained by rumpling, a reduced phase is also observed experimentally on the Sr-O columns that lie exactly on the mirror plane (see Fig. 4), and this is not reproduced by the simulated images from the model, since it exhibits no rumpling on the mirror plane. Vacancies were next considered as a potential cause of this decrease. Since the original reported model of Benedek *et al.*[5] did not include vacancies, additional DFT calculations were performed to refine the model structure with vacancies included.

The original DFT relaxed structure reported by Benedek *et al.*[5] fully optimized the internal coordinates, in the sense of minimizing the total energy; the excess volume per unit area was calculated by optimizing the length of the c axis (which is perpendicular to the interface in the models). Following optimization, the effects of Sr and O vacancies were considered. Two Sr (O) vacancies were created on the Sr-Ti-O planes furthest from either side of the interfaces (there were two GBs per simulation cell because of periodic boundary conditions) and the internal coordinates were again fully optimized; the c-axis length was held fixed. In a separate, pristine (but relaxed) model, two Sr (O) vacancies were created on the GB planes (one on each GB). The internal coordinates were optimized and the c-axis length was held fixed. The segregation energy, E_{seg} is then given by,

$$E_{\text{seg}} = E_{\text{bulk}} - E_{\text{GB}}, \tag{1}$$

where E_{GB} is the total energy of the GB with the vacancies on the GB plane and E_{bulk} is the total energy of the GB with the vacancies in the bulk. Care was taken to ensure that the two vacancies in each simulation cell were the same distance apart in both the GB and bulk calculations. This precaution is especially necessary when the vacancies are charged so that

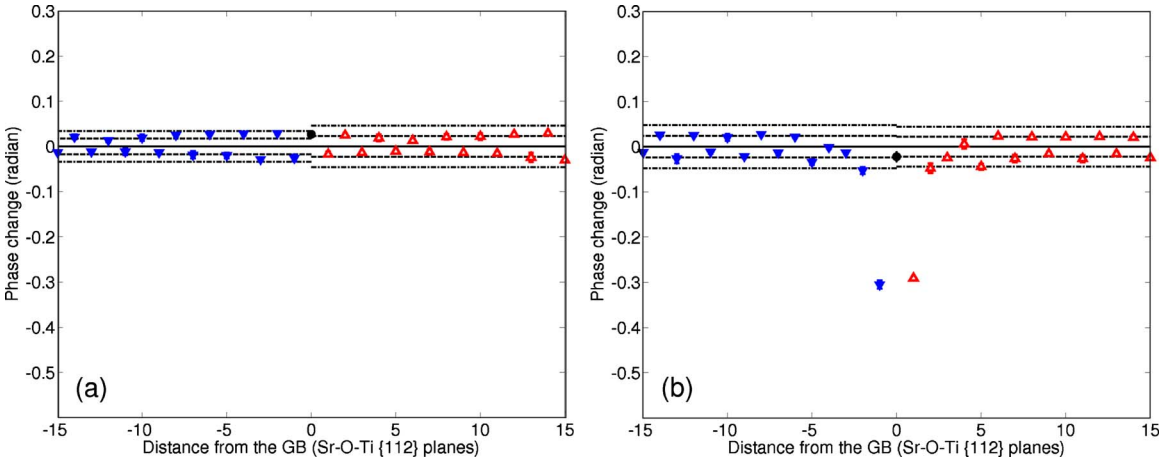

FIG. 5. (Color online) Phase change with respect to mean bulk Sr-O column phase plotted as a function of distance from the GB for (a) the unrelaxed GB model and (b) the DFT relaxed mirror symmetric model structure. Plot symbols as in Fig. 4.

TABLE II. Phase change measured on Sr-O columns for three rumpling values calculated from simulated exit wave phases with respect to the phase on the unrumpled column.

Rumpling (Å)	Phase change (rad)
$r=0.3$	-0.14 ± 0.003
$r=0.5$	-0.27 ± 0.003
$r=0.8$	-0.42 ± 0.003

the spurious electrostatic interactions introduced by periodic boundary conditions are eliminated from the segregation energy. Positive energies indicate a preference for segregation.

The segregation energy for the neutral Sr vacancy to the $\Sigma3$ (112) $[\bar{1}10]$ mirror symmetric boundary was calculated to be 0.23 eV while the segregation energy for the −2 charged Sr vacancy was calculated to be 0.28 eV. The segregation energy for the neutral O vacancy to the $\Sigma3$ (112) $[\bar{1}10]$ mirror symmetric boundary was calculated to be −0.08 eV while the segregation energy for the +2 charged O vacancy was calculated to be −0.87 eV. This analysis shows that segregation of Sr vacancies to the GB is energetically favorable while O vacancy segregation is not.

Following the DFT analysis of vacancy segregation energy, a refined model structure that included both Sr-O rumpling on the planes adjacent to the mirror plane and Sr vacancies on the mirror plane was generated. Including 20% Sr vacancies on the mirror plane led to a phase change of (-0.40 ± 0.003) rad, consistent with the experimentally measured decrease, as shown in Table I. Therefore, it is suggested that a concentration of 20% Sr vacancies segregated to the boundary mirror plane would lead to phase changes consistent with the experimentally measured values for the Sr-O columns on the boundary mirror plane. Figure 6 plots the Sr-O column phase data the refined DFT model overlayed with the average experimentally measured data. From this figure it concluded that the experimentally observed boundary structure is consistent with the refined structure, which includes both rumpling and vacancies.

V. DISCUSSION AND CONCLUSIONS

Quantitative exit wave-function phase analysis demonstrates that excellent agreement between the refined DFT model structure and the experimentally observed boundary structure has been achieved when both Sr-O rumpling adjacent to the boundary plane (as predicted by DFT calculations) and 20% Sr vacancies on the boundary plane were included. However, it is also possible that effects such as surface layers or grain-boundary grooving could lead to decreases consistent with the experimental data. Such options cannot be completely ruled out from the analysis presented here. However, by averaging Sr-O column pixel values from several, independent thin areas of the specimen, as was done here, the significance of these effects can be minimized. Further, as discussed in Sec. III, it was found that phase changes resulting from tilting the simulation model structures or from different postreconstruction higher-order aberration-correction values did not significantly impact the quantitative results.

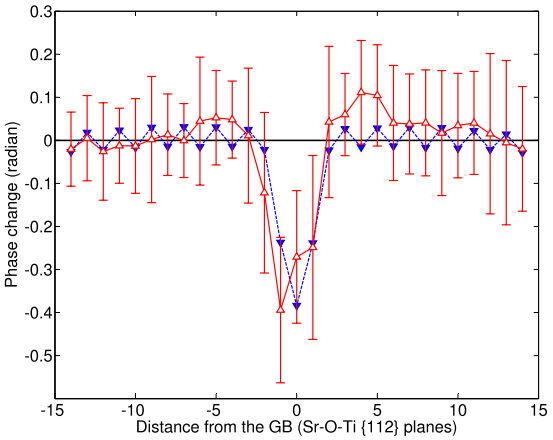

FIG. 6. (Color online) Comparison of phase change with respect to mean bulk Sr-O columns plotted as a function of distance from the GB as measured for the experimental data (open triangles) and refined DFT model (filled triangles).

Using aberration-corrected HRTEM and focal series reconstruction, experimental and theoretical GB structures have been compared. The exit wave-function phase data measured on specific columns has been used as a "fingerprint" for the boundary structure. By performing detailed quantitative analysis on reconstructed and simulated exit wave phases, statistically significant phase changes have been measured for Sr-O columns on specific planes. By comparison with DFT relaxed model structures, it has been possible to differentiate between two proposed structures not significantly different in their calculated energies, and to deduce three-dimensional information about the atomic arrangement near the GB plane. Without structural relaxation information provided by DFT, in particular, the rumpling of planes adjacent to the boundary, it would not be possible to produce such three-dimensionally refined GB structures. In such cases, vacancies would be the primary explanation for reduced phase values measured on atomic columns. DFT calculations verified that the segregation of Sr vacancies is a plausible explanation of the reduction in phase shifts measured on the boundary plane while rumpling accounts for the reduction on neighboring planes without the need to postulate vacancies there.

ACKNOWLEDGMENTS

The authors thank U. Salzberger for assistance with sample preparation and A. Chua and A. Sutton for helpful discussions. Financial support by the EC under Contract No. NMP3-CT-2005-013862 (INCEMS) is acknowledged. K.J.D. thanks NSERC and the University of Oxford, Clarendon Fund for financial support.

*Present address: Cornell Center for Materials Research, Cornell University, Ithaca, NY 14853, USA.
†Corresponding author; david.cockayne@materials.ox.ac.uk

[1] W. M. Rainforth, Adv. Imag. Elect. Phys. **132**, 167 (2004).
[2] O. Kienzle, M. Exner, and F. Ernst, Phys. Status Solidi A **166**, 57 (1998).
[3] S. Hutt, S. Kostlmeier, and C. Elsässer, J. Phys.: Condens. Matter **13**, 3949 (2001).
[4] R. Astala and P. D. Bristowe, J. Phys.: Condens. Matter **14**, 13635 (2002).
[5] N. A. Benedek, A. L. S. Chua, C. Elsässer, A. P. Sutton, and M. W. Finnis, Phys. Rev. B **78**, 064110 (2008).
[6] A. Strecker, J. Mayer, B. Baretzky, U. Eigenthaler, T. Gemming, R. Schweinfest, and M. Rühle, J. Electron Microsc. **48**, 235 (1999).
[7] M. Haider, S. Uhlemann, E. Schwan, H. Rose, B. Kabius, and K. Urban, Nature (London) **392**, 768 (1998).
[8] L. Y. Chang, A. I. Kirkland, and J. M. Titchmarsh, Ultramicroscopy **106**, 301 (2006).
[9] C. L. Jia, M. Lentzen, and K. Urban, Microsc. Microanal. **10**, 174 (2004).
[10] N. A. Benedek and M. W. Finnis, GROT*:* a program for determining grain misorientations by a quaternion fit, 2008, the FORTRAN90 code is available on request from M. W. Finnis or N. A. Benedek.
[11] M. J. Hÿtch and W. M. Stobbs, Microsc. Microanal. Microstruct. **5**, 133 (1994).
[12] K. J. Dudeck and D. J. H. Cockayne, J. Phys.: Conf. Ser. (to be published).
[13] W. O. Saxton, Ultramicroscopy **55**, 171 (1994).
[14] W. O. Saxton, T. J. Pitt, and M. Horner, Ultramicroscopy **4**, 343 (1979).
[15] R. R. Meyer, A. I. Kirkland, and W. O. Saxton, Ultramicroscopy **92**, 89 (2002).
[16] A. Thust, M. H. F. Overwijk, W. M. J. Coene, and M. Lentzen, Ultramicroscopy **64**, 249 (1996).